The Influence of Sea Ice and Snow Cover and Nutrient Availability on the Formation of Massive Under-Ice Phytoplankton Blooms in the Chukchi Sea

Jinlun Zhang

Carin Ashjian

Robert Campbell

Yvette H. Spitz

Michael Steele

See next page for additional authors

Authors

Jinlun Zhang, Carin Ashjian, Robert Campbell, Yvette H. Spitz, Michael Steele, and Victoria Hill

The influence of sea ice and snow cover and nutrient availability on the formation of massive under-ice phytoplankton blooms in the Chukchi Sea

Jinlun Zhang [a,*], Carin Ashjian [b], Robert Campbell [c], Yvette H. Spitz [d], Michael Steele [a], Victoria Hill [e]

[a] University of Washington, United States
[b] Woods Hole Oceanographic Institution, United States
[c] University of Rhode Island, United States
[d] Oregon State University, United States
[e] Old Dominion University, United States

ARTICLE INFO

ABSTRACT

A coupled biophysical model is used to examine the impact of changes in sea ice and snow cover and nutrient availability on the formation of massive under-ice phytoplankton blooms (MUPBs) in the Chukchi Sea of the Arctic Ocean over the period 1988–2013. The model is able to reproduce the basic features of the ICESCAPE (Impacts of Climate on EcoSystems and Chemistry of the Arctic Pacific Environment) observed MUPB during July 2011. The simulated MUPBs occur every year during 1988–2013, mainly in between mid-June and mid-July. While the simulated under-ice blooms of moderate magnitude are widespread in the Chukchi Sea, MUPBs are less so. On average, the area fraction of MUPBs in the ice-covered areas of the Chukchi Sea during June and July is about 8%, which has been increasing at a rate of 2% yr^{-1} over 1988–2013. The simulated increase in the area fraction as well as primary productivity and chlorophyll a biomass is linked to an increase in light availability, in response to a decrease in sea ice and snow cover, and an increase in nutrient availability in the upper 100 m of the ocean, in conjunction with an intensification of ocean circulation. Simulated MUPBs are temporally sporadic and spatially patchy because of strong spatiotemporal variations of light and nutrient availability. However, as observed during ICESCAPE, there is a high likelihood that MUPBs may form at the shelf break, where the model simulates enhanced nutrient concentration that is seldom depleted between mid-June and mid-July because of generally robust shelf-break upwelling and other dynamic ocean processes. The occurrence of MUPBs at the shelf break is more frequent in the past decade than in the earlier period because of elevated light availability there. It may be even more frequent in the future if the sea ice and snow cover continues to decline such that light is more available at the shelf break to further boost the formation of MUPBs there.

1. Introduction

Arctic sea ice extent has decreased dramatically in recent years, particularly in the Pacific sector of the Arctic Ocean including the Chukchi Sea (e.g., Serreze et al., 2007; Stroeve et al., 2012; Comiso, 2012). This ice decrease is in response to increasing air temperatures, changes in ocean heat transport, increased storminess, reduced cloudiness, and increased penetration of solar radiation into the upper ocean (e.g., Perovich et al., 2008; Kay et al, 2008; Steele et al., 2010; Overland et al., 2012; Zhang et al., 2013; Parkinson and Comiso, 2013). With the increased sea ice melt in the Arctic, the proportion of first year ice relative to older, thicker ice in the Pacific sector is much greater than before (e.g., Kwok, 2007; Maslanik et al., 2007, 2011; Stroeve et al., 2012). First year sea ice is not only relatively thin but also more susceptible to the development of melt ponds, both of which transmit more light to the underlying water column (e.g., Light et al., 2008; Frey et al., 2011). Warmer air temperatures also promote more rapid and earlier melting of snow from the surface of the sea ice, which increases penetration of light (Nicolaus et al. 2012). More light penetration not only increases the input of heat, warming the upper water column and strengthening stratification, but also

* Corresponding author.
E-mail address: zhang@apl.washington.edu (J. Zhang).

promotes greater primary production (e.g., Mundy et al., 2009). Greater primary production, observed by satellite for open water areas and simulated in models for both open water and ice-covered areas, has been found in recent years in response to the decreased sea ice extent and longer phytoplankton growing season, particularly in the Chukchi Sea (e.g., Arrigo et al., 2008; Zhang et al., 2010a).

Despite its extreme polar conditions, the Chukchi Sea is ranked among the most productive seas in the world (e.g., Gosselin et al., 1997; Hill and Cota, 2005). Light, temperature, and nutrients govern the variability of the biological productivity in the Chukchi Sea, as in other Arctic peripheral seas (Andersen, 1989; Smith and Sakshaug, 1990; Gosselin et al., 1997; Hill and Cota, 2005; Lee and Whitledge, 2005). The vast shallow continental shelf of the Chukchi Sea serves as a link between the Pacific and the Arctic oceans. Pacific water, a major source of buoyancy and nutrients to the Arctic Ocean, flows over the Chukchi shelf (Woodgate et al., 2005; Weingartner et al., 2005; Codispoti et al., 2005). Advection of Pacific water, upwelling/downwelling along the shelf break, and cross-shelf exchanges between shelf and basin influence biological and chemical distributions and processes in the Chukchi Sea.

In early July 2011, the ICESCAPE (Impacts of Climate on the Eco-Systems and Chemistry of the Arctic Pacific Environment) project observed a massive phytoplankton bloom in the northern Chukchi Sea > 100 km north of the ice edge (Arrigo et al., 2012, 2014). The occurrence of this massive under-ice phytoplankton bloom (MUPB) is attributed to increased penetration of light to the upper ocean through thin ice and melt ponds (Arrigo et al., 2012, 2014; Palmer et al., 2014) and ocean dynamics such as upwelling in the shelf break areas (e.g., Pickart et al., 2013; Spall et al., 2014). Satellite-based analysis deduced that under-ice phytoplankton blooms, defined by chlorophyll a (chl a) values above a threshold of 2.5 mg m^{-3} at the time of sea ice retreat from a location, are widespread in the Chukchi Sea and have been prevalent there for more than a decade prior to the 2011 ICESCAPE discovery (Lowry et al., 2014).

Here we focus on two overarching questions: (1) What is the spatiotemporal variability of MUPBs in the Chukchi Sea? (2) What is the role of changes in sea ice and snow cover and nutrient availability in the formation of MUPBs? We conducted a numerical investigation of the integrated system of the sea ice and snow cover, the ocean, and marine planktonic ecosystem in the Chukchi Sea over the period 1988–2013 using the coupled pan-arctic **B**iology/**I**ce/**O**cean **M**odeling and **A**ssimilation **S**ystem (**BIOMAS**). Our focus is on MUPBs which are defined hereafter by chl a values exceeding a threshold of 10 mg m^{-3}, although the study also describes the existence of under-ice phytoplankton blooms of lower magnitude (such as above a threshold of 2.5 mg m^{-3} as identified in Lowry et al., 2014). This threshold of 10 mg m^{-3} is somewhat arbitrary. However, a change in the threshold, by ± 5 mg m^{-3}, does not change the basic outcome of this study.

2. Model description

2.1. Model elements

BIOMAS is a coupled biophysical model (Zhang et al., 2010a, 2014) that has three model elements: a sea ice model, an ocean circulation model, and a pelagic biological model. The pelagic biological model is an 11-component marine pelagic ecosystem model that includes two phytoplankton components (diatoms and flagellates), three zooplankton components (microzooplankton, copepods, and predator zooplankton), dissolved organic nitrogen, detrital particulate organic nitrogen, particulate organic silica, nitrate, ammonium, and silicate (see Fig. 3 in Zhang et al., 2014;

also see Kishi et al., 2007). Values of key biological parameters used in the model are listed in Zhang et al. (2010a). The model does not simulate sea ice algae.

The ocean circulation model is based on the Parallel Ocean Program (POP) developed at Los Alamos National Laboratory (Smith et al., 1992). The POP ocean model is modified by Zhang and Steele (2007) so that open boundary conditions can be specified. The POP ocean model is further modified by Zhang et al. (2010b) to incorporate tidal forcing arising from the eight primary constituents (M2, S2, N2, K2, K1, O1, P1, and Q1) (Gill, 1982). The tidal forcing consists of a tide generating potential with corrections due to both the earth tide and self-attraction and loading following Marchuk and Kagan (1989).

The sea ice model is a thickness and enthalpy distribution (TED) sea ice model (Zhang and Rothrock, 2003; Hibler, 1980). The TED sea ice model has eight categories each for ice thickness, ice enthalpy, and snow depth. The centers of the eight ice thickness categories are 0, 0.38, 1.30, 3.07, 5.97, 10.24, 16.02, and 23.41 m (also see Zhang et al., 2010b). Thus the first category is actually the open water category, while the other seven categories represent ice of various thicknesses. It is adopted from the **P**an-arctic **I**ce/**O**cean **M**odeling and **A**ssimilation **S**ystem (PIOMAS; Zhang and Rothrock, 2003) and able to assimilate satellite observations of sea ice concentration, following Lindsay and Zhang (2006), and sea surface temperature (SST), following Manda et al. (2005) (also see Schweiger et al., 2011).

The model estimates the attenuation of photosynthetically active radiation (PAR) in the water column following $PAR(z) = PARfrac \times E_0 \exp[(-\alpha_1 - \alpha_S PF - \alpha_L PD)z]$, where $PARfrac$ is the fraction of net shortwave radiation that is photosynthetically active, E_0 is the area mean net shortwave radiation on the ocean surface, α_1, α_S, and α_L are light attenuation coefficients due to seawater and flagellates and diatoms, and z is depth (see Zhang et al., 2010a). E_0 is the area weighted average of net shortwave radiation over each of the open water and ice categories calculated by the sea ice model following Maykut and Untersteiner (1971) and Hibler (1980). For open water, net shortwave radiation is directly applied to the ocean surface; for ice categories of various thicknesses, net shortwave radiation is allowed to penetrate through snow and sea ice, with an attenuation coefficient of 20 m^{-1} for snow (Grenfell and Maykut, 1977) and 1.5 m^{-1} for ice (Maykut and Untersteiner, 1971). Note that the sea ice model does not yet include a melt pond parameterization, although we plan to implement this in the future. The value of $PARfrac$ ranges from 0.39 to 0.53 globally (Pinker and Laszlo, 1992), reflecting the fact that only part of the solar radiation spectrum is available for photosynthesis. For simplicity, we use a constant value of $PARfrac = 0.43$ for this study (Zhang et al., 2010a).

2.2. Model configuration

The BIOMAS model domain covers the Northern Hemisphere north of 39°N (Fig. 1a). The BIOMAS finite-difference grid is based on a generalized orthogonal curvilinear coordinate system with a horizontal dimension of 600×300 grid points. The "north pole" of the model grid is placed in Alaska. Thus, BIOMAS has its highest horizontal resolution along the Alaskan coast and in the Chukchi, Beaufort, and Bering seas. For the Chukchi and Beaufort seas, the model resolution ranges from an average of 4 km in the Alaska coastal areas to an average of ~ 10 km for the whole region (Fig. 1b). There are 26 ocean grid cells across Bering Strait for a good connection between the Pacific Ocean and the Arctic Ocean. To better resolve the mixed layer and the pycnocline, the ocean's vertical dimension has 30 levels of different thicknesses, with 13 levels in the upper 100 m, the top six of which are 5 m thick. The model bathymetry (Fig. 1b) is obtained by merging the IBCAO
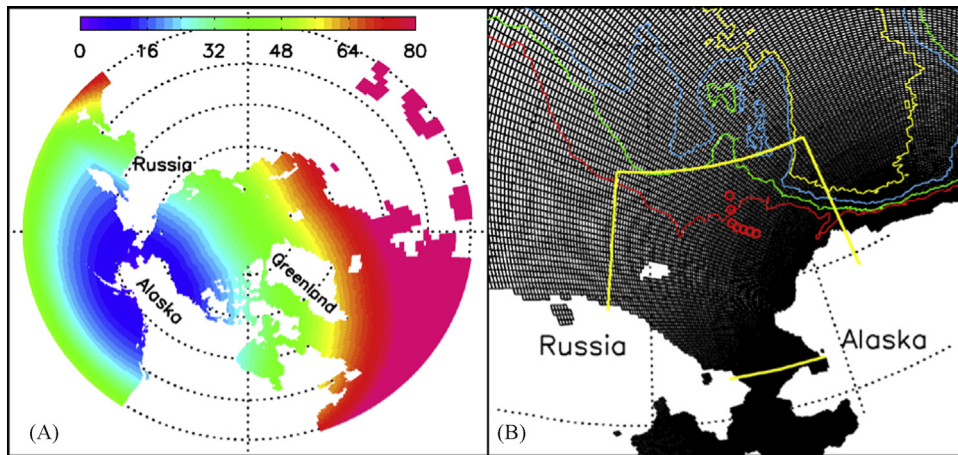
Fig. 1. BIOMAS model grid configuration showing (a) the entire model domain, consisting of the Arctic, North Pacific, and North Atlantic oceans and (b) the subdomain of the Chukchi, Beaufort, and East Siberian seas. The model domain covers all ocean areas north of 39ºN. The colors in (a) indicate the model's varying horizontal resolution in km (see color key at top of panel). In (b), the red, green, blue, and yellow lines represent isobaths of 100, 500, 2200, and 3600 m, respectively. The circles in (b) represent the locations of ICESCAPE stations 46 (southernmost circle) through 57 (northernmost circle) along transect 1 defined in Arrigo et al. (2012). The area encircled by thick yellow lines, bounded by 175ºE, –155ºW, 66.6ºN, and 75ºN, is defined roughly as the Chukchi Sea for the purpose of analysis. (For interpretation of the references to color in this figure legend, the reader is referred to the web version of this article.)

(International Bathymetric Chart of the Arctic Ocean) dataset and the ETOPO5 (Earth Topography Five Minute Gridded Elevation Data Set) dataset (see Holland 2000).

The modification of the POP ocean model to allow open boundary conditions enables BIOMAS, a regional model, to be one-way nested to a global coupled sea ice–ocean model (Zhang, 2005). The global model's outputs of ocean velocity, temperature, salinity, and sea surface height are used as open boundary conditions for the southern boundaries of the BIOMAS domain along 39°N. In addition, the nitrate and silicate along the open boundaries (which are far away from the Arctic Ocean) are restored to monthly climatology data from the *World Ocean Atlas 2005* (Garcia et al., 2006) by the same method as Zhang et al. (2014).

BIOMAS is integrated from 1971 to 2013, driven by daily NCEP/NCAR reanalysis surface atmospheric forcing (Kalnay et al., 1996). The atmospheric forcing consists of surface winds, air temperature, specific humidity, precipitation, evaporation, and downwelling longwave radiation and cloud fraction. Cloud fraction and surface air temperature are used to calculate surface downwelling shortwave radiation following Parkinson and Washington (1979). Initial conditions for the BIOMAS integration consist of January 1, 1971 fields of sea ice and ocean state variables obtained from a PIOMAS integration that starts from 1948 (Zhang et al., 2008) and January mean climatology fields of nitrate and silicate from the *World Ocean Atlas 2005* (Garcia et al., 2006). Initial conditions also include a uniform distribution (0.02 mmol N m^{-3}; 0.02 mmol Si m^{-3}) of plankton and other biogeochemical components in the upper 200 m following Zhang et al. (2010a). Results over the period 1988–2013 are presented here.

3. Results

3.1. Daily evolution of modeled under-ice primary productivity, chl a, nutrient availability, and PAR

In this subsection, we examine the general characteristics of the modeled daily evolution of primary productivity (PP), chl *a*, nutrient availability, and PAR at the ocean surface or in the ocean surface layer (0–5 m, also referred to as 'at surface' hereafter) by focusing on long-term climatological daily means in the ice-covered areas of the Chukchi Sea (Fig. 2). Ice-covered areas were
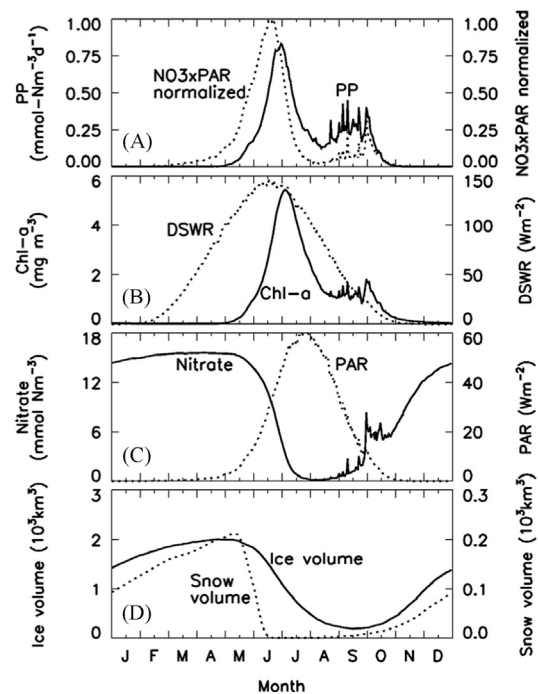

Fig. 2. 1988–2013 mean daily evolution of (a) PP and the multiplication of nitrate concentration and photosynthetically active radiation (PAR) normalized by the maximum value of the multiplication defined as: (nitrate × PAR)/max (nitrate × PAR), (b) chl *a* concentration and downward shortwave radiation (DSWR), and (c) nitrate concentration and PAR in the ice-covered areas (ice concentration above 15%) of the Chukchi Sea defined by the areas within the yellow lines in Fig. 1, and (d) sea ice and snow volumes in the Chukchi Sea. PP, chl *a*, and nitrate are in the ocean surface layer (0–5 m), PAR is at the ocean surface, and DSWR is at the surface of either sea ice or snow. (For interpretation of the references to color in this figure legend, the reader is referred to the web version of this article.)

identified for each day by selecting grid points from the model where ice cover was present (ice concentration above 15%) in the Chukchi Sea, roughly defined by the region encircled by thick yellow lines in Fig. 1b. The currency of the biological model component is nitrogen (mmol N m^{-3}), which needs to be converted to carbon (C) and chl *a* for model–observation comparisons. We follow Lavoie et al. (2009) to use a fixed C:N (mol:mol) ratio of 106:16 (Redfield et al., 1963) and a fixed N:chl *a* (wt:wt) ratio of
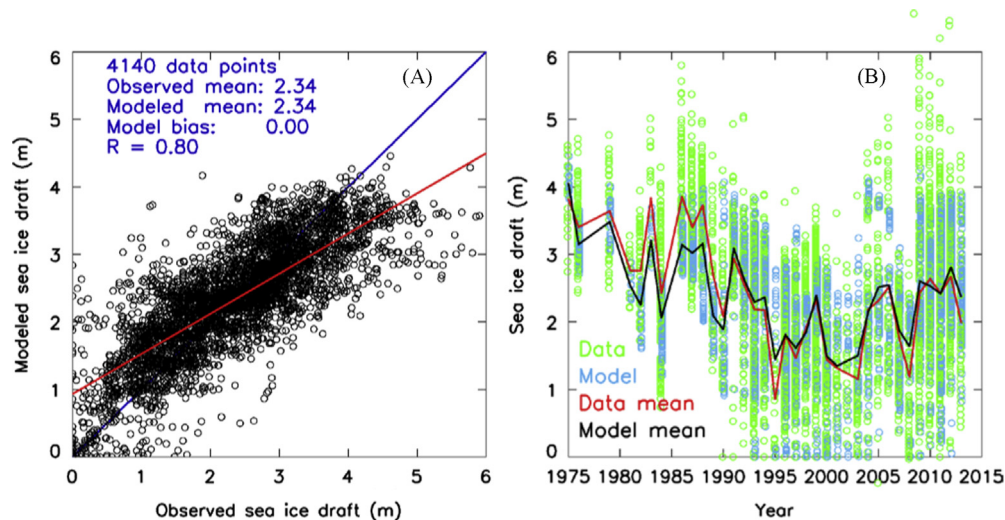
Fig. 3. (a) A comparison of model simulated sea ice draft with available sea ice draft (or thickness converted to draft) observations over the period of 1975–2013 available from the Sea Ice Climate Data Record (CDR, http://psc.apl.washington.edu/sea_ice_cdr/, Lindsay, 2010, 2013). The observations include those from submarine-based upward looking sonars (ULS) over much of the central Arctic Basin (Rothrock et al., 2008), from moored ULS in the Chukchi and eastern Beaufort seas (Melling and Riedel, 2008), in the central Beaufort Sea (The Beaufort Gyre Exploration Project, Krishfield et al., 2014), and in Fram Strait area (Witte and Fahrbach, 2005), from airborne electromagnetic induction instruments (Haas et al., 2009), and from the airborne laser altimeters of the NASA Operation IceBridge Project (Kurtz et al., 2013). The IceBridge data are sea ice thickness data, which are converted into draft data by simply dividing by 1.12. The electromagnetic data are combined ice and snow thickness data, which are converted to draft data using modeled snow depth following Rothrock et al. (2008). The blue line indicates equality and the red line represents the best fit to the observations. The number of total observation points, model and observation mean values, model bias (mean model-observation difference), and model-observation correlation (R) are listed. (b) Observations and corresponding model results (circles) for those individual years with observations available and annual observation and model means (lines). (For interpretation of the references to color in this figure legend, the reader is referred to the web version of this article.)

8.75:1 for the unit conversions. We focus on the surface properties because the ICESCAPE data suggest that, although subsurface chl a maxima exist, MUPBs are most likely to occur at or near the surface (Arrigo et al., 2012, 2014). Before May, there is no surface PP under ice, averaged over the period 1988–2013, in the Chukchi Sea (Fig. 2a). PP increases rapidly in June and peaks near the end of the month before rapidly decreasing in July. In September and October, PP tends to rebound, but with much smaller, less well defined peaks.

The daily evolution of surface chl a under ice is similar to that of PP, except that chl a peaks about 4 days later (Fig. 2b). The modeled under-ice blooms are not likely to occur before June or after July, if we follow Lowry et al. (2014) to define under-ice blooms as those with chl a values above the threshold of 2.5 mg m^{-3}, but without the need for a time-component because, unlike satellites, the model reveals blooms under the ice as well as in open water. In June and July, under-ice blooms are common in the Chukchi Sea with mean chl a values often exceeding 2.5 mg m^{-3}, consistent with the findings of Lowry et al. (2014). Fig. 2b also suggests that most of MUPBs are likely to occur only after mid-June and before mid-July, as this is the period when maximum chl a biomass is attained.

High surface nitrate concentration is seen in late fall (fall defined as October–December), winter (January–March), and most of spring (April–June), except June in the ice-covered areas of the Chukchi Sea (Fig. 2c). The high concentrations seen before June are likely due to a combination of nutrient regeneration in the benthos during winter (see a review by Anderson, 1995), input of nutrient-rich Pacific water entering through Bering Strait (e.g., Codispoti et al., 2005; Grebmeier and Harvey, 2005), and upwelling in the shelf break regions that brings nutrient-rich waters from deep offshore basins onto the shelves (e.g., Carmack and Wassmann, 2006; Carmack et al., 2006; Pickart et al., 2009, 2011, 2013; Codispoti et al., 2005, 2013; Spall et al., 2014). Nitrate concentration decreases rapidly in June and is almost completely depleted by July–September, because of uptake in under-ice phytoplankton blooms. In contrast, PAR at the ocean surface

increases rapidly in June and peaks in late July before decreasing thereafter (Fig. 2c).

To roughly assess the combined effect of nutrient availability and PAR on under-ice phytoplankton growth, Fig. 2a shows the daily evolution of nitrate concentration multiplied by PAR and normalized by the maximum value of the multiplication, defined by (nitrate × PAR)/max (nitrate × PAR). Needless to say, the combined effect so defined does not completely reflect the complicated, nonlinear interactions among light, nutrients, and biological processes. It is used here only as a simplified measure of the combined effect, which is the highest near the middle of June, about 10–15 days before the PP peak (Fig. 2a). This suggests that June conditions play an important role in under-ice blooms, particularly MUPBs.

The influence of sea ice and snow cover on light transmission is shown by a comparison between PAR at the ocean surface under ice (Fig. 2c) and downward shortwave radiation at the surface of ice or snow (DSWR, Fig. 2b). Although DSWR may be greater than 100 W m^{-2} in May, there is little PAR because thick ice and snow largely prevents DSWR from reaching the ocean surface (Fig. 2d). In June, sea ice starts to decrease quickly and snow is completely melted (Fig. 2d). As a result, PAR climbs most rapidly (Fig. 2c). Sea ice continues to retreat in July and August and therefore PAR continues to grow and peaks in late July, even though DSWR peaks in June.

3.2. Changes in sea ice and snow cover and PAR and comparison with observations

Given the importance of sea ice and snow in altering light transmission, model performance in simulating sea ice and snow is examined to verify that the model results are realistic and appropriately replicate natural conditions. Model simulated sea ice draft is compared with various sources of sea ice draft observations collected over the period of 1975–2013, available from the Sea Ice Climate Data Record (CDR, see Lindsay, 2010, 2013) (Fig. 3). Overall,
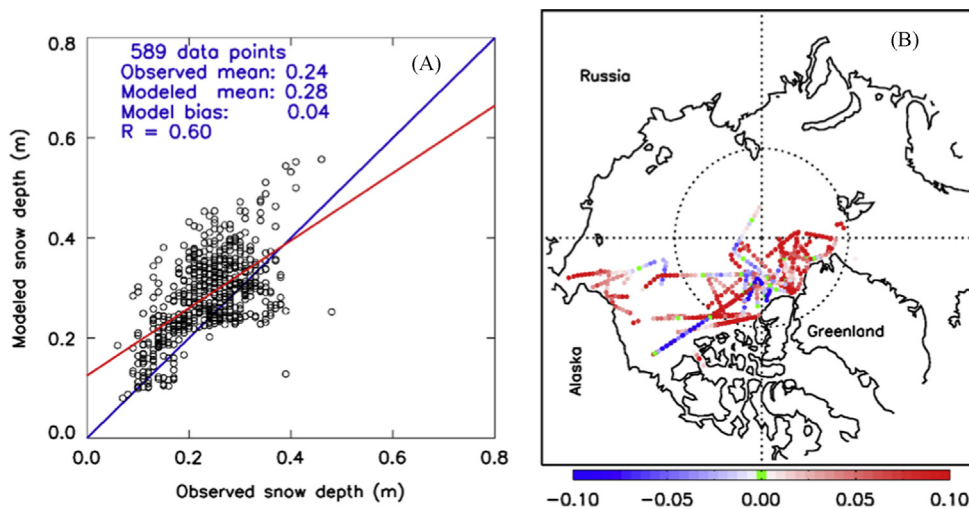
Fig. 4. (a) A comparison of available snow depth (m) data from the NASA IceBridge program collected during March and/or April of 2009–2012. The IceBridge snow depth data are obtained from the Sea Ice CDR (Lindsay, 2010, 2013). (b) Point-by-point snow depth differences (m) between model results and observations. All observations in the Chukchi Sea were made in March 2012.

the model compares well with the available observations (4140 data points in total) over the period 1975–2013 with a zero mean bias and high correlation ($R=0.80$), although some individual points may show discrepancies of up to several meters (Fig. 3a). The model captures most of the ups and downs of the annual mean values of ice draft observations, suggesting that the model is able to reproduce the observed interannual variability reasonably well (Fig. 3b).

Snow depth observations in the Arctic Ocean are particularly sparse. However, snow depth data collected by the NASA IceBridge mission during March and/or April of 2009–2012 are available from the Sea Ice CDR and compared with model results (Fig. 4). A comparison between the available snow depth observations (589 data points in total) and the corresponding model results shows a mean model bias of 0.04 m (or 17% against observed mean value of 0.24 m), with a correlation of $R=0.60$ (Fig. 4a). The limited IceBridge data in the Chukchi Sea were collected during March 2012 (Fig. 4b). A comparison of model output vs. observations indicates that the model overestimates snow depth in the Southern Chukchi Sea, while it performs better in the northern Chukchi Sea (Fig. 4b).

Over the period 1988–2013, the model simulated June sea ice extent in the Chukchi Sea is close to satellite observed ice extent every year except 1988 (Fig. 5a). This is no surprise, given that the model assimilates satellite sea ice concentration following Lindsay and Zhang (2006). Here we focus on conditions in June since they are most likely to directly impact the formation of MUPBs, as shown in Fig. 2. Both model results and satellite observations show a generally downward trend in June ice extent over 1988–2013 (Fig. 5a; Table 1). There is also a general downward trend in the simulated June sea ice and snow volumes in the Chukchi Sea (Fig. 5b; Table 1). However, the simulated snow volume is subject to relatively large interannual fluctuations from near zero in 1990 to 0.08×10^3 km^3 in 1999, and stays generally low since 2006, except in 2010 (Fig. 5b).

As sea ice in June declines, PAR generally increases over 1988–2013, with relatively high values in the past decade (Fig. 5c; Table 1). In particular, PAR stays relatively high in the past decade or so because of a mostly low sea ice and snow cover. Changes in PAR in June are highly correlated with the changes in the corresponding sea ice volume ($R=-0.88$). They are also correlated with those in snow volume, though to a lesser degree ($R=-0.65$). A particularly noticeable effect of snow cover on PAR is in 1990

when the simulated PAR reaches a local maximum in response to a near snow-free June. The particularly low PAR in 1988, 1994, and 1995 is due to high ice extent (Fig. 5a) and high ice and snow volumes (Fig. 5b).

3.3. Changes in PP, chl a, and nutrient availability and comparisons with observations

The simulated monthly mean surface chl a is compared with the MODIS-Terra observed monthly composite surface chl a, averaged over the period 2001–2012, for ice-free areas of the Arctic Ocean (Fig. 6) to evaluate the model's performance in simulating the lower trophic level of the ecosystem. Model simulated ice-free areas or ice-covered areas are close to satellite observations, since the model simulated ice edges almost overlap the satellite observed ice edges (Fig. 6). This is largely due to model assimilation of satellite ice concentration (see also Fig. 5a).

In ice-free areas, the model captures the basic spatial pattern of chl a estimated using MODIS observations during May–August. Both model results and observations show generally higher chl a concentration in the coastal areas and on the Chukchi, Beaufort, East Siberian, Laptev, and Kara shelves (Fig. 6). Although model results are generally within the range of the MODIS observations in the open water areas, the model underestimates or overestimates surface chl a from time to time and from location to location relative to the satellite estimates. For example, the model overestimates surface chl a in the Greenland Sea in May (Fig. 6a and b), while underestimates it in Laptev and Kara seas in August (Fig. 6g and h). Also, the model has a tendency to overestimate surface chl a in the open water areas of the northern Bering in June (Fig. 6c and d) and southern Chukchi Sea in July (Fig. 6e and f). The discrepancies may be linked to model overestimation or underestimation of light and nutrient distributions and to model uncertainties in parameters such as phytoplankton photoinhibition and photochemical reaction coefficients and zooplankton grazing and mortality rates (also see Zhang et al., 2010a, 2014). The discrepancies may be also linked to the fact that the model results are monthly mean values, while the satellite data are monthly composite values.

The model generates high surface chl a concentration in some ice-covered areas where MODIS chl a data are not available because data retrievals are hindered by the ice cover (Fig. 6a–f). The simulated high
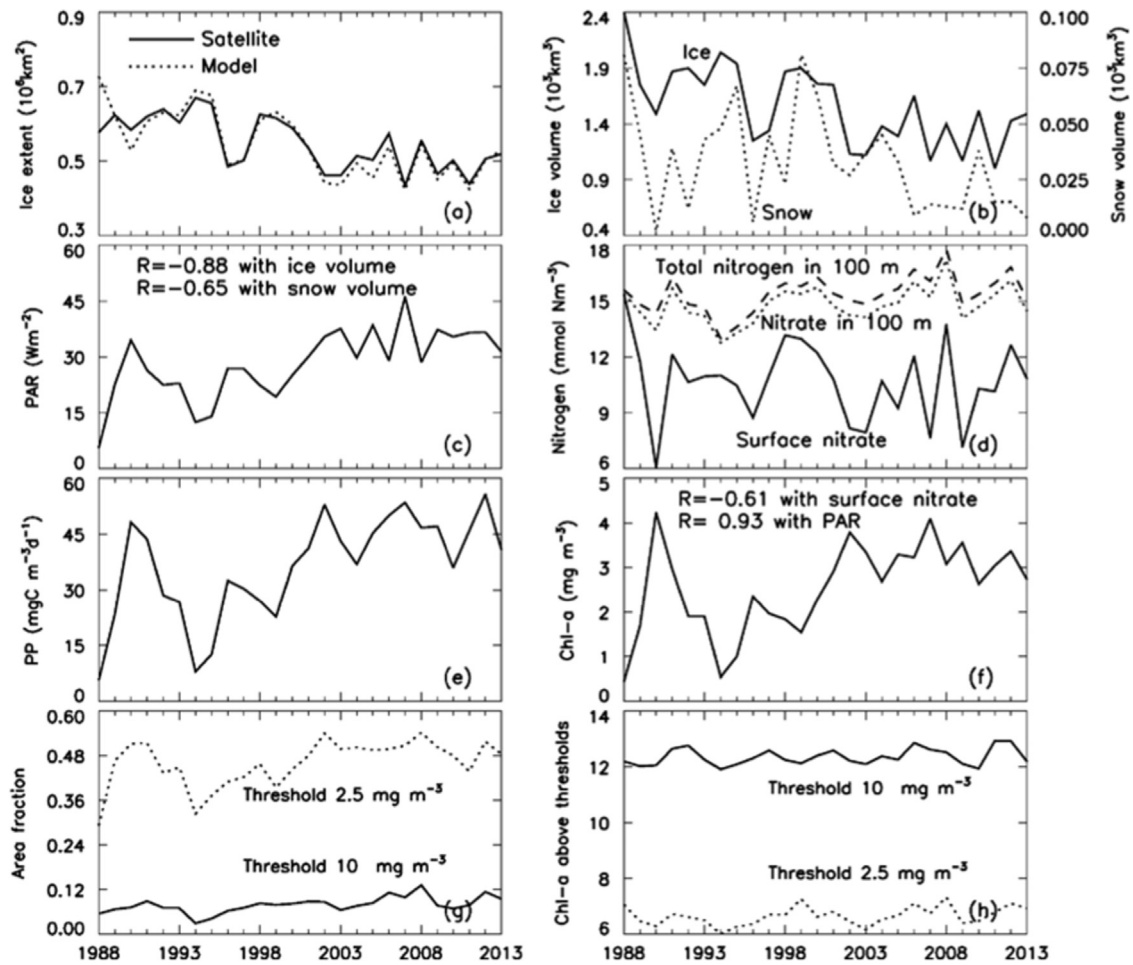
Fig. 5. Simulated and observed June sea ice extent (a) and simulated June sea ice and snow volumes (b) in the Chukchi Sea. Simulated June PAR at the ocean surface (c), nitrate concentration at the surface and in the upper 100 m and total nitrogen (sum of phytoplankton, zooplankton, nitrate, detrital particulate organic nitrogen, and ammonium) in the upper 100 m (d), and PP and chl *a* in the ocean surface layer (e and f) in the ice-covered areas of the Chukchi Sea. Simulated area fraction with chl *a* concentration values exceeding a threshold of 2.5 mg m^{-3} or 10 mg m^{-3} in ice-covered areas (g) and chl *a* concentration averaged over those chl *a* concentration values exceeding a threshold of 2.5 mg m^{-3} or 10 mg m^{-3} (h) during June and July in the ice-covered areas of the Chukchi Sea. Some correlation (*R*) values are listed in (c) and (f).

Table 1

1988–2013 mean and linear trends for variables shown and described in Fig. 5. Bold numbers exceed the 95% confidence level when tested in a way that accounts for temporal autocorrelation. The unit for column four (Trend/|mean| × 100%) is % yr^{-1}.

	Mean	Trend	Trend/|mean| × 100%	Unit of trend
Satellite ice extent	0.55	**−0.0062**	**−1.12**	10^6 km^2 yr^{-1}
Model ice extent	0.55	**−0.0079**	**−1.43**	10^6 km^2 yr^{-1}
Ice volume	1.56	**−0.030**	**−1.92**	10^3 km^3 yr^{-1}
Snow volume	0.033	**−0.0013**	**−3.94**	10^3 km^3 yr^{-1}
PAR	28.2	**0.81**	**2.87**	W m^{-2} yr^{-1}
Surface nitrate concentration	10.7	−0.043	−0.40	mmol N m^{-3} yr^{-1}
Nitrate concentration in upper 100 m	14.8	0.047	0.32	mmol N m^{-3} yr^{-1}
Total nitrogen concentration in upper 100 m	15.4	**0.059**	**0.38**	mmol N m^{-3} yr^{-1}
Primary productivity	36.2	**1.16**	**3.20**	mg C m^{-3} d^{-1} yr^{-1}
Chl *a*	2.56	**0.072**	**2.81**	mg m^{-3} yr^{-1}
Area fraction with chl *a* > 2.5 mg m^{-3}	0.46	**0.0041**	**0.89**	yr^{-1}
Area fraction with chl *a* > 10 mg m^{-3}	0.079	**0.0016**	**2.03**	yr^{-1}
Mean chl *a* over areas with chl *a* > 2.5 mg m^{-3}	6.66	0.014	0.21	mg m^{-3} yr^{-1}
Mean chl *a* over areas with chl *a* > 10 mg m^{-3}	12.35	0.012	0.09	mg m^{-3} yr^{-1}

under-ice chl *a* concentrations occur mainly on or near the shelves in the Pacific sector of the Arctic Ocean, especially in the Chukchi Sea. Under-ice phytoplankton blooms may occur as early as May in the Chukchi Sea, mainly near the coast (Fig. 6a), with surface chl *a* concentration values exceeding 2.5 mg m^{-3} (Lowry et al., 2014). In June and July, under-ice blooms are widespread in the Chukchi Sea (Fig. 6c and e). However, as shown in Fig. 2b, MUPBs (chl *a* concentration values above 10 mg m^{-3}) are most likely to occur

between mid-June and mid-July. In August onward, the likelihood of developing under-ice blooms diminishes (Fig. 6g).

Model results are further compared with SBI (the Shelf Basin Interactions Program) and SHEBA (the Surface Heat Budget of the Arctic Ocean Program) in situ observations of PP and chl *a* and nitrate concentrations. The model is able to capture the timing of spring blooms at SBI stations and along the SHEBA tracks. Model results are also generally within the range of the SBI and SHEBA
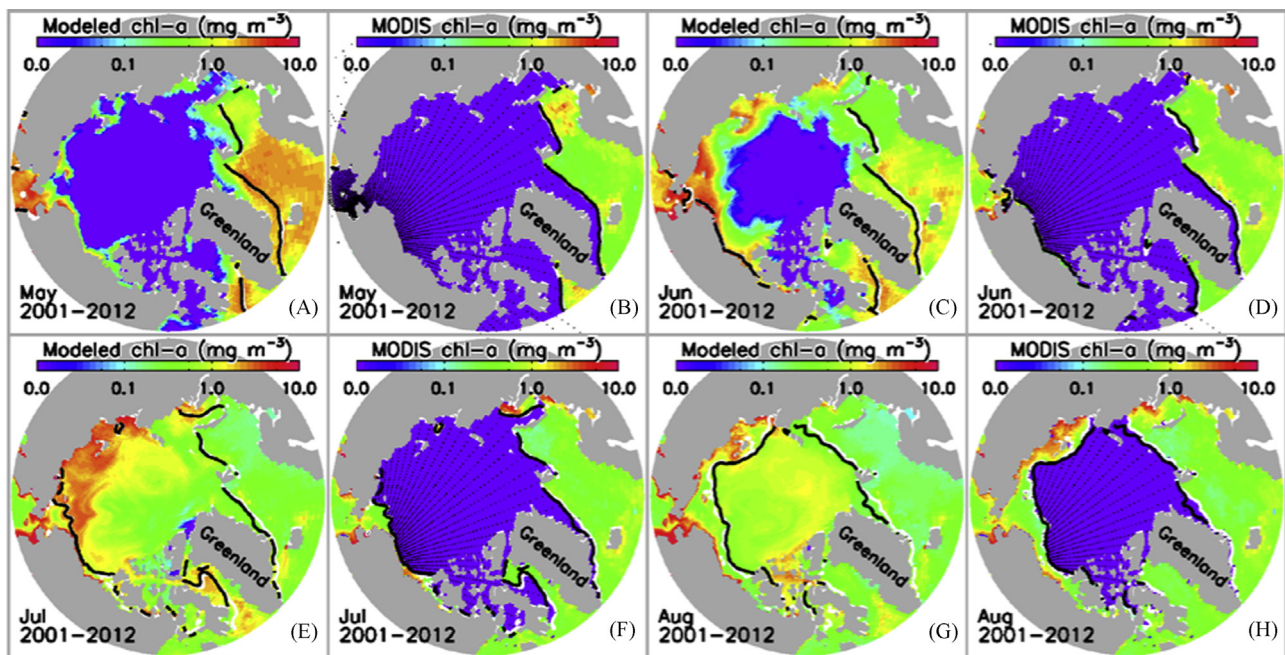
Fig. 6. Model simulated monthly mean and MODIS-Terra observed monthly composite surface concentration of chlorophyll *a* (chl *a*), averaged over the period 2001–2012. The white line represents satellite observed monthly mean sea ice edge defined as 0.15 ice concentration and black line model simulated ice edge, also averaged over the period 2001–2012. There are almost no MODIS chl *a* data under ice (dotted areas). MODIS chl *a* data are available from http://oceancolor.gsfc.nasa.gov/. Satellite ice concentration data are from http://nsidc.org/data/nsidc-0081.html.

in situ observations. These comparisons are similar to those in Zhang et al. (2010a) and not shown here.

Over the period 1988–2013, the model simulated surface PP and chl *a* in June in the ice-covered areas of the Chukchi Sea show an increasing trend (Fig. 5e and f; Table 1), particularly after the early 1990s, because of generally declining sea ice and snow cover and increasing light availability (Fig. 5a–c; Table 1). The strong effect of light availability on under-ice chl *a* is demonstrated by high correlation ($R = 0.93$) between chl *a* concentration and PAR (Fig. 5f). There is a sharp peak of PP and chl *a* in 1990, which is linked to the disappearance of snow cover (Fig. 5b) and associated increase in light transmission to the water column (Fig. 5c). This suggests the importance of snow cover in influencing biological processes.

To a lesser degree, the simulated surface chl *a* concentration is also correlated ($R = -0.61$) with surface nitrate concentration in June over 1988–2013 (Fig. 5d and f). The negative correlation value is obviously an indication that phytoplankton growth consumes nutrients. The surface nitrate concentration is further correlated with ice volume ($R = 0.68$, not shown in Fig. 5), indicating that sea ice cover plays a role in the variations of nutrient availability through oceanic, optical, and biological processes. There is a negative trend in surface nitrate concentration (Table 1), which may be linked to reduced sea ice and snow cover (increased ice and snow melt) and increased PAR and phytoplankton growth in recent years. However, the negative trend is relatively small and not statistically significant (Table 1).

There is a positive trend in the simulated nitrate concentration and total nitrogen concentration (sum of phytoplankton, zooplankton, nitrate, detrital particulate organic nitrogen, and ammonium) in the upper 100 m in June (Fig. 5d). This is consistent with the finding of Zhang et al. (2010a) that the decline in Arctic sea ice tends to increase the nutrient availability in the euphotic zone, often in the Chukchi and Beaufort seas, by enhancing air–sea momentum transfer, leading to strengthened upwelling and mixing in the water column and therefore increased nutrient input into the upper ocean layers from below. Particularly, recent

observations indicate increases in Ekman convergence and downwelling in the Canada Basin in association with increasing sea ice retreat and melt (McLaughlin and Carmack, 2010) that are linked to an intensified Beaufort gyre (e.g., Proshutinsky et al., 2009; Yang, 2009; McPhee, 2013). As downwelling increases in the Canada Basin, upwelling in the shelf break areas of the Basin is likely to increase as well, leading to a general increase in nutrient availability on the shelves, including the Chukchi Sea. The positive trend in nutrient availability in the Chukchi Sea is likely to help boost biological production in the region.

3.4. Changes in massive under-ice phytoplankton blooms and comparisons with observations

The model is able to capture the basic features of the ICESCAPE observed vertical distribution of particulate organic carbon (POC) under ice or in the open water areas along transect 1 (stations 46–57) as defined in Arrigo et al. (2012) (Fig. 7a and b). In particular, the model reproduces the ICESCAPE observed MUPB at close to the correct location and time, at station 56 during 3–4 July 2011 (Fig. 7b), where ice concentration is near or above 80% (Fig. 7a). The model is also able to create a subsurface maximum in the open water area as seen in the ICESCAPE data (stations 46–52).

However, the simulated magnitude of the MUPB at station 56 is about 12% lower and the location of the simulated subsurface maximum is shallower in the water column than the observations. In addition, the model tends to underestimate POC at depth, which may be one of the reasons that the model overestimates nitrate concentration in the deeper ocean layers (Fig. 7c) because it underestimates biological consumption of nutrients there. The model is in better agreement with observations of nitrate concentration in the upper ocean, where nutrients are mostly depleted during July 3–4. The model-observation differences are likely due to insufficient modeled light penetration through ice/snow and water column. One way to increase the light availability in the water column in the model is to introduce melt ponds for enhanced light

penetration (e.g., Fetterer and Untersteiner, 1998; Light et al., 2008; Frey et al., 2011). This may improve the model's ability to better simulate MUPBs (e.g., Arrigo et al., 2012; Palmer et al., 2014).
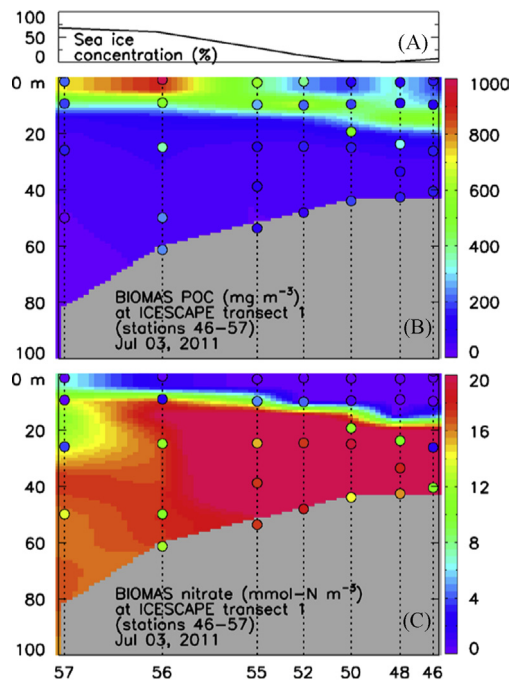

Fig. 7. Simulated sea ice concentration (a) and vertical profiles of particulate organic carbon (POC) (b) and nitrate (c) for July 3 of 2011 at ICESCAPE stations 46 (southernmost circle) through 57 (northernmost circle) along transect 1 defined in Arrigo et al. (2012) (also see Fig. 1). The colored circles represent the values of the ICESCAPE observations at the stations. (For interpretation of the references to color in this figure legend, the reader is referred to the web version of this article.)

The model simulation of the spatial extent of the ICESCAPE-observed MUPB along transect 1 is further illustrated in the surface chl *a* field on 3 July 2011 (Fig. 8f). Along the ICESCAPE transect across the Chukchi Sea ice edge, model results show reduced surface chl *a* concentration at the stations in the open water area to the south, elevated concentration at the stations north of the ice edge, highest concentration at station 56 (the second northernmost station along transect 1), and a lower concentration again at or just north of station 57 (the northernmost station), which is further into the ice pack. These results are generally in good agreement with observations, as also shown in Fig. 7.

Satellite-based analysis indicates that under-ice phytoplankton blooms occur not only in 2011, but also in other years in the Chukchi Sea (Lowry et al., 2014). This is reflected in Fig. 8, which further shows that modeled MUPBs also occur in other years. However, the simulated MUPBs appear to be temporally sporadic and spatially patchy. For example, MUPBs are widespread on 3 July 1991 (Fig. 8a), whereas there are few on the same day in 1995 (Fig. 8b). Also, although being sporadic and patchy, MUPBs often occur along or near the 100 and 500 m isobaths in the Chukchi Sea (Fig. 8a and c–f), suggesting that upwelling along the shelf break is important to sustaining the bloom (e.g., Pickart et al., 2013; Spall et al., 2014). In addition, MUPBs tend to form in the shelf break areas more frequently in recent years (Fig. 8c–f) than in the earlier period (Fig. 8a–c). In particular, almost no MUPBs are simulated in the shelf break areas in 1995 and 1999.

According to the model, the area fraction of MUPBs (> 10 mg m^{-3}) in the ice covered areas of the Chukchi Sea during June and July is 8%, while the area fraction of all under-ice blooms (> 2.5 mg m^{-3}) is 46% during that time (Fig. 5g; Table 1). Both area fractions have statistically significant positive trends (Table 1), particularly since the early 1990s, reflecting the decrease in sea ice and snow cover and the increase in light and nutrient availability. The magnitudes of both MUPBs and all under-ice blooms also show positive trends (Fig. 5h), although these do not exceed the 95% confidence level (Table 1).
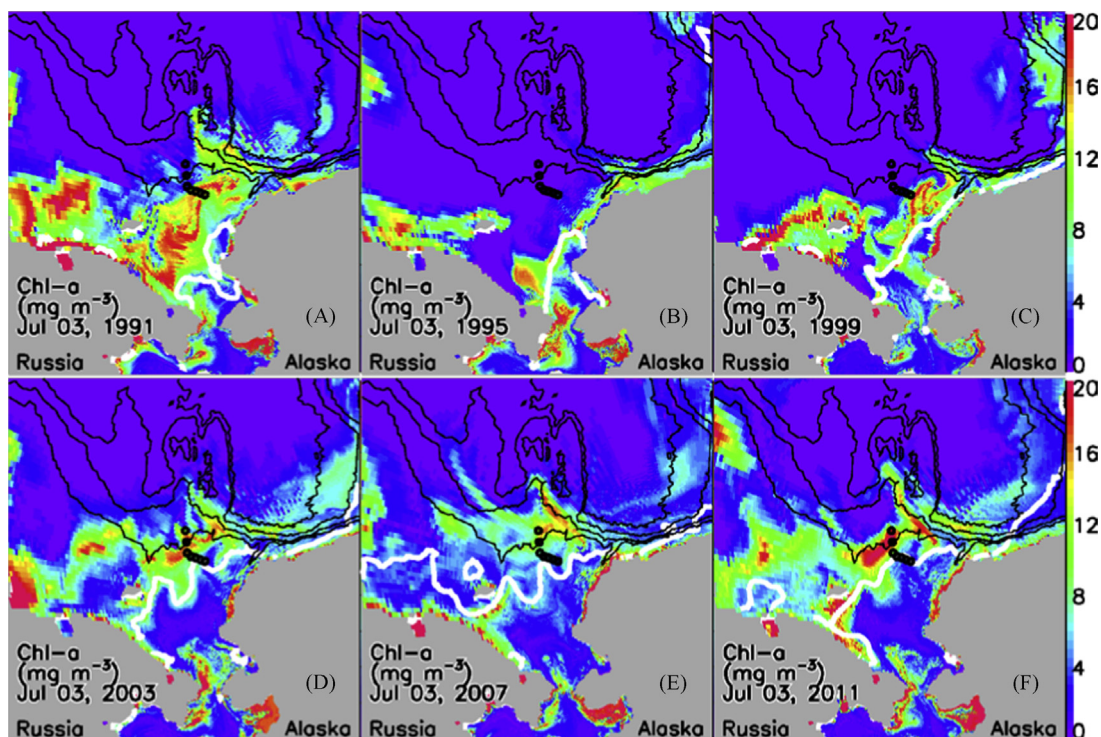

Fig. 8. Simulated July 3 mean surface chl *a* concentration for six evenly spaced years including the ICESCPAE year of 2011. The white line represents satellite observed ice edge. ICESCAPE stations 46–57 along transect 1 are marked by circles (also see Fig. 1). Thin black lines represent isobaths of 100, 500, 2200, and 3600 m, respectively.
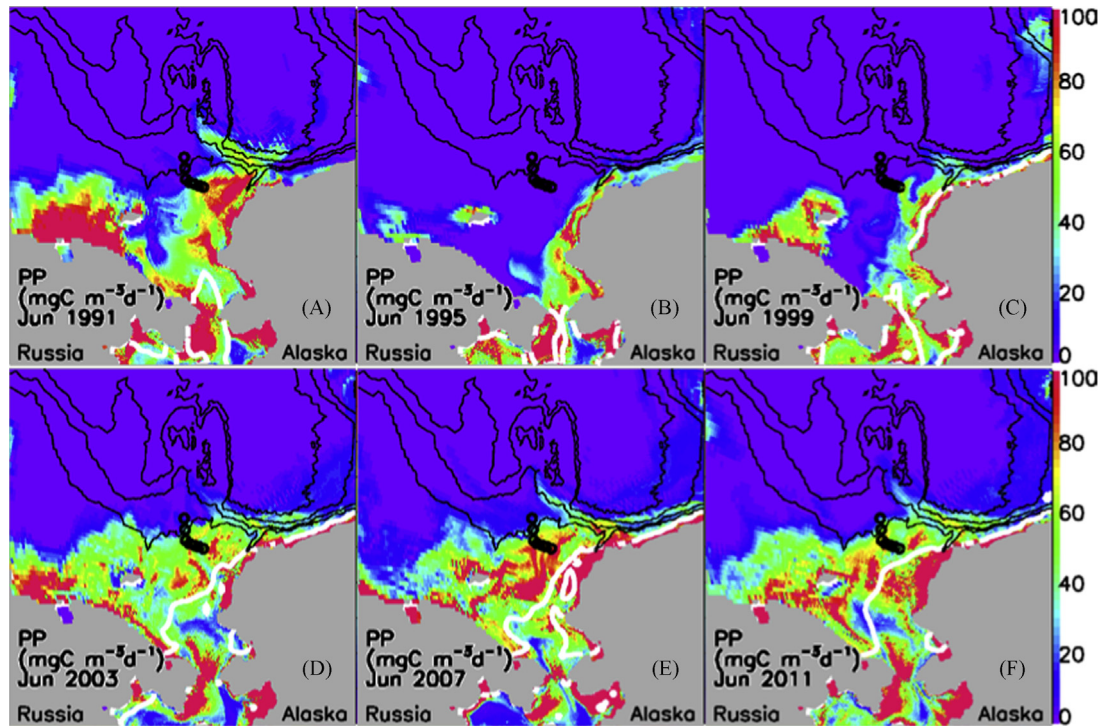
Fig. 9. Simulated June mean surface primary productivity (PP) (mg C m^{-3} d^{-1}) for six evenly spaced years.
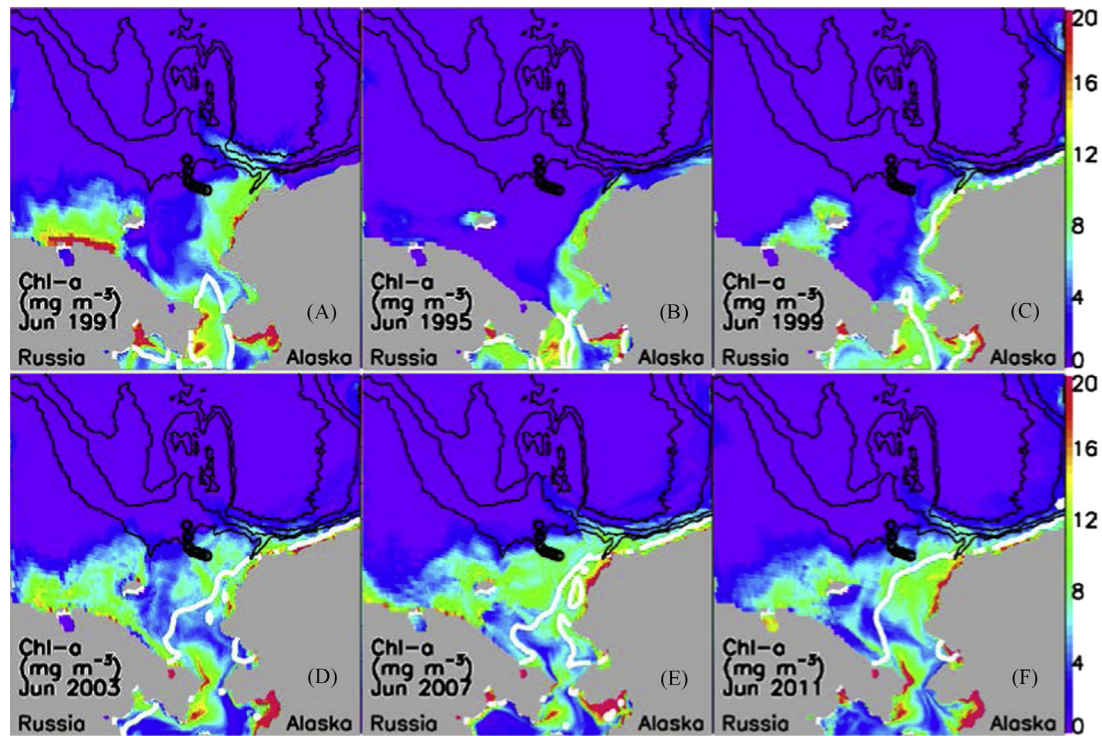

Fig. 10. Simulated June mean surface chl a (mg m^{-3}) for six evenly spaced years.

3.5. Spatiotemporal conditions for massive under-ice phytoplankton blooms

For this analysis, we examine the spatial distributions of the parameters driving the formation and maintenance of MUPBs by focusing on six years of the analysis between 1991 and 2011, spaced four years apart. PP and chl a in June are generally higher in recent years (especially in 2003, 2007, and 2011) relative to the 1990s in the ice-covered areas of the Chukchi Sea (Figs. 9 and 10). Some of the chl a concentration values exceed the threshold of 10 mg m^{-3} in these areas. Correspondingly, the simulated sea ice and snow cover is generally thinner, less compact, and of smaller extent in the recent years than in the 1990s (Figs. 11 and 12). As a result, light availability has increased (Fig. 13). The simulated under-ice PAR is often as high as 90 W m^{-2} in surface waters, extending far north into the ice pack even near the 100 m isobath (Fig. 13d–f). In the
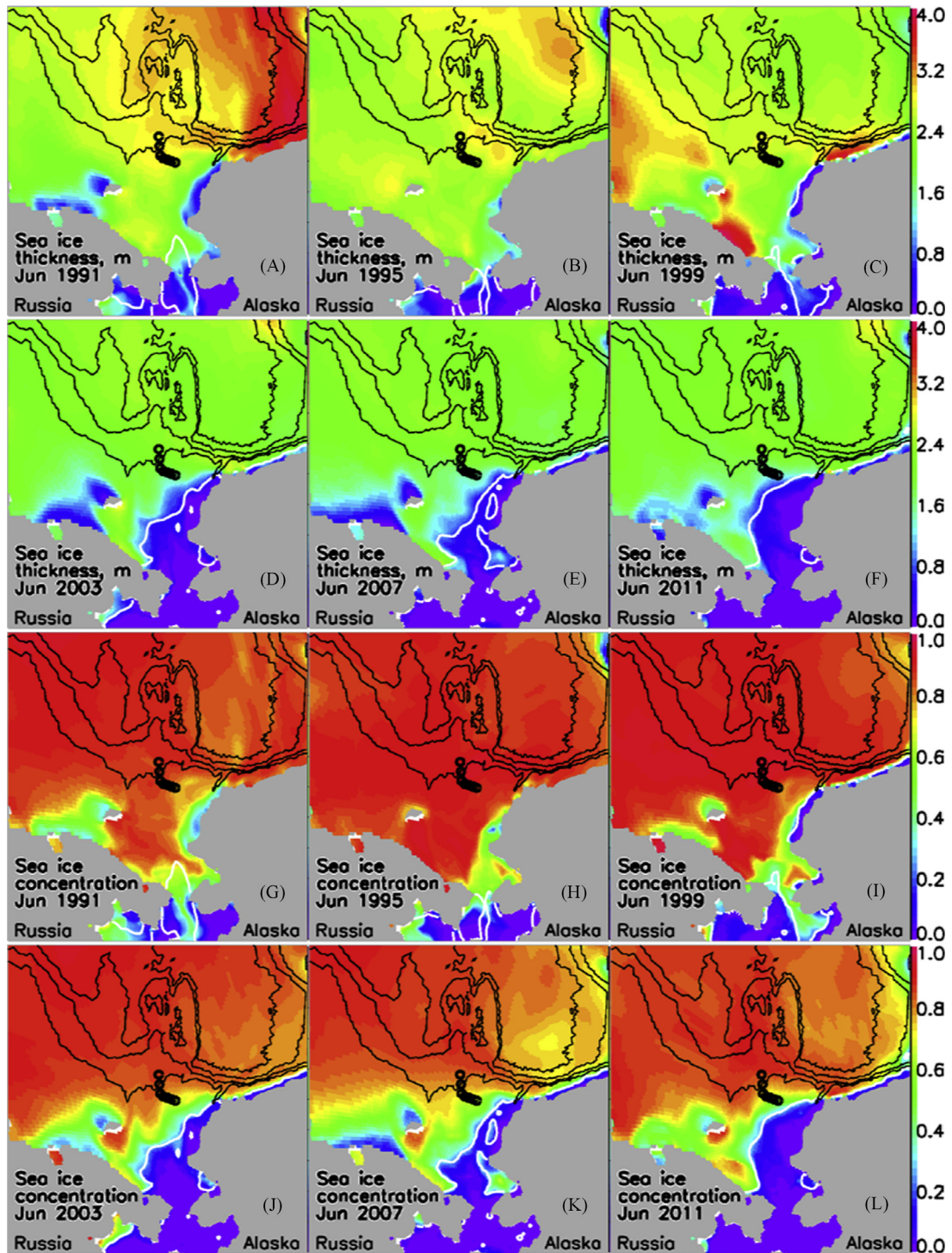
Fig. 11. Simulated June mean sea ice thickness (m) (a–f) and concentration (g–l) for six evenly spaced years.

1990s, in contrast, PAR is lower everywhere except in the coastal areas or in the south, particularly in 1995 (Fig. 13b) when there is a thicker, more compact ice and snow cover in much of the Chukchi Sea (Fig. 11b, h, and 12b). The low PAR in 1995 leads to near zero PP and chl *a* concentration over much of the region (Figs. 9b and 10b) where there is little chance to form MUPBs (Fig. 8b).

The simulated June surface nitrate concentration in the Chukchi Sea is generally lower in recent years than in the 1990s (Fig. 14). This is consistent with the negative trend (although not statistically significant) in surface nitrate concentration, while there is a positive trend in the nitrate concentration and total nitrogen concentration in

the upper 100 m (Fig. 5d; Table 1). As mentioned earlier, the decreasing trend in the surface nitrate concentration is linked to increasing biological consumption with higher PP and phytoplankton biomass in recent years (Fig. 5e and f; Table 1).

One of the key features of the simulated spatial distribution of surface nitrate concentration is that relative high nitrate concentration often occurs along or near the 100 and 500 m isobaths in the Chukchi Sea (Fig. 14). This is, as mentioned before, likely due to upwelling and other oceanic processes such as vertical mixing and horizontal advection etc. in the shelf break areas (e.g., Pickart et al., 2013). The frequent formation of MUPBs in shelf break areas in June is associated
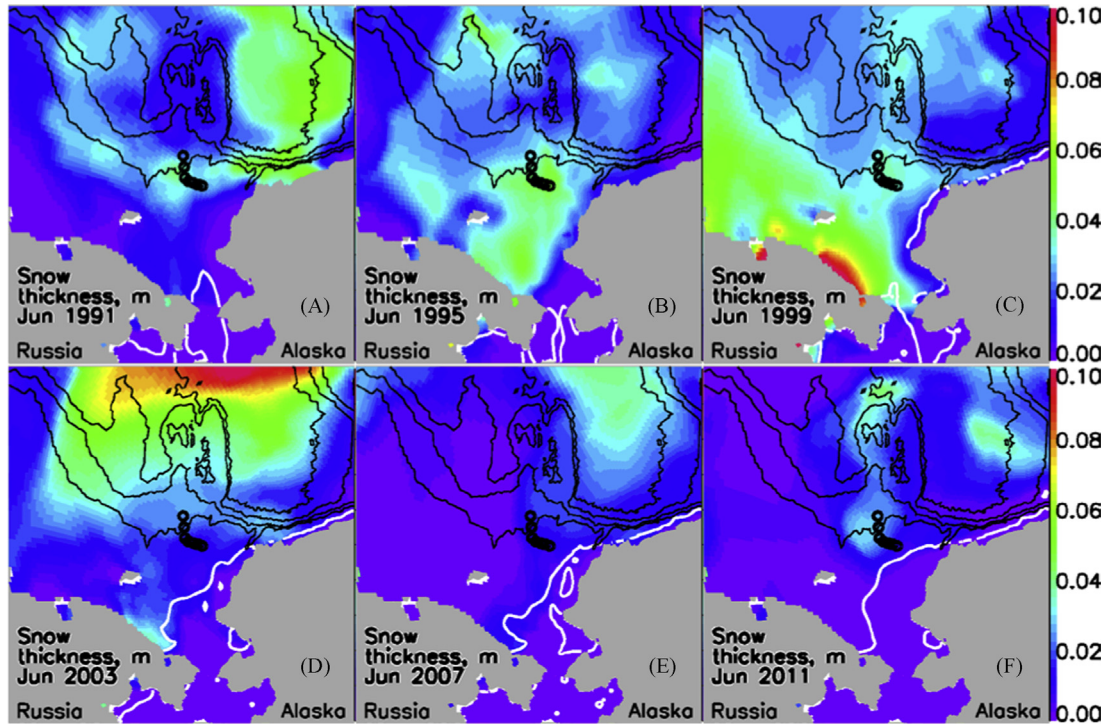
Fig. 12. Simulated June mean snow depth (m) for six evenly spaced years.
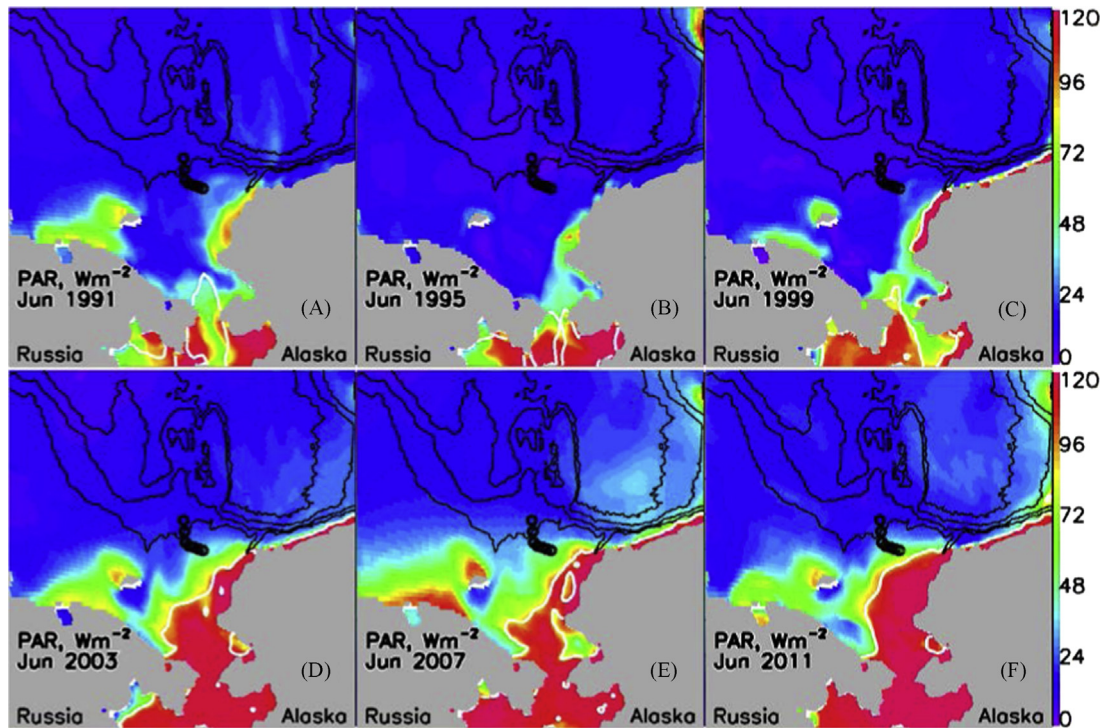

Fig. 13. Simulated June mean photosynthetically active radiation (PAR) (W m^{-2}) at the ocean surface six evenly spaced years.

with relatively high nitrate concentrations found there, not only in the 2000s and 2010s, but also in some of the earlier years such as 1991 (Fig. 8). In particular, the 2011 ICESCAPE MUPB (Arrigo et al., 2012, 2014; also see model results in Figs. 7 and 8f) is located close to the 100 m isobath where the simulated nitrate concentration remains high in June (Fig. 14f).

Other mechanisms may also change nutrient availability and influence phytoplankton growth on the shelf. Nutrients upwelled at the shelf break may spread more widely onto the shelf (Spall et al., 2014), which, together with winter nutrient regeneration and the inflow of nutrient rich Pacific water, contributes to the often high nitrate concentration on the interior shelf (Fig. 14).
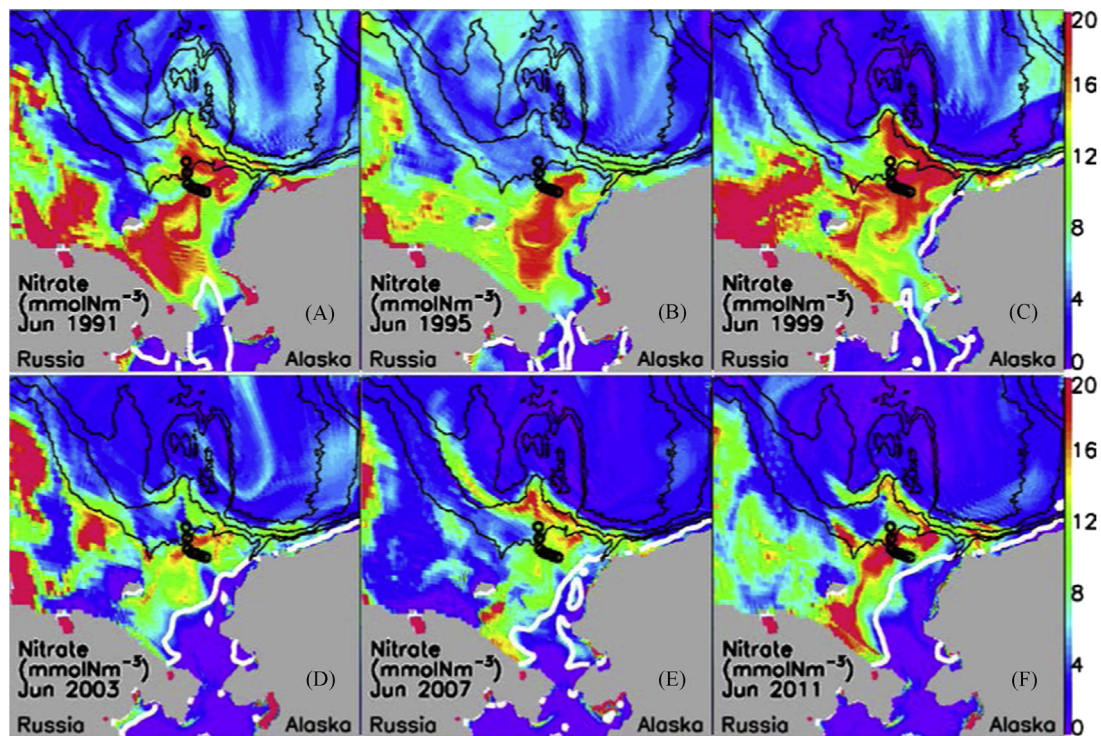
Fig. 14. Simulated June mean surface nitrate concentration (mmol N m^{-3}) for six evenly spaced years.

The nutrient-rich Pacific water inflow is seen particularly in 2011, where elevated nitrate in the southern and western Chukchi Sea follows the known pathway of northward advection of Pacific water along the coast of Anadyr (Fig. 14f). In June 1991, nitrate concentration remains high in much of the central Chukchi Sea (Fig. 14a) where phytoplankton growth is strong (Figs. 9a and 10a), even though the simulated PAR is not high (Fig. 13a). As a result, MUPBs are widespread in the region on 3 July 1991 (Fig. 8a).

Thus, on the one hand, the simulated MUPBs are sporadic and patchy because of the strong spatiotemporal changes in light and nutrient availability. On the other hand, there is high probability of occurrence of MUPBs in the shelf break areas where nutrients may not be depleted during mid-June and mid-July, particularly in recent years with decreasing sea ice and snow cover such that enhanced light availability may reach the shelf break areas (Fig. 13d–f).

4. Concluding remarks

We have used the BIOMAS biophysical model to investigate the influence of sea ice and snow cover and nutrient availability on the formation of MUPBs in the Chukchi Sea of the Arctic Ocean over the past two and half decades. The coupled biophysical model is able to realistically simulate sea ice thickness and extent, snow depth, and variations of PP and chl a and nitrate concentration in the Arctic Ocean. This is demonstrated through comparisons with satellite, in situ, and airborne observations, although model over-estimation or underestimation may occur at some times or locations. In particular, it captures the basic features of the ICESCAPE observed MUPB in July 2011, at the appropriate time and location. The model's underestimation, to some degree, of the magnitude of the MUPB at ICESCAPE station 56 and the general underestimation of observed POC at depth not only at station 56 but also at other stations may suggest the necessity of introducing melt pond parameterization into the model to enhance light penetration through ice and into the water column.

According to the model, the Chukchi Sea is characterized prominently by a steep decrease in sea ice and snow cover in June, often being snow free by late June, which greatly elevates light availability. This triggers a rapid increases of PP and chl a concentration and drawdown of nutrients. Though only simple metric, the multiplication of nitrate concentration and PAR is illustrative of the prominent actions occurring in June. As a combined effect of PAR and nutrient supply, there is a sharp peak of PP and chl a concentration at the end of June and in early July. The sharpness and the magnitude of the chl a concentration peak suggests that MUPBs are most likely to occur between mid-June and mid-July.

As suggested by satellite data (Lowry et al., 2014), model results show that under-ice blooms occur not only in the ICESCAPE year of 2011, but also in previous years. This is also true with MUPBs, according to the model. Model results further show that under-ice blooms are widespread in the Chukchi Sea, with a mean area fraction of 0.46 during June–July over the period 1988–2013. This is in contrast to MUPBs with a mean area fraction of a mere 0.08 or 8%. Although small in magnitude, the simulated area fraction of MUPBs has been increasing at a rate of 2.0% yr^{-1} over 1988–2013. The increase in the area fraction is concurrent with an increase in the simulated surface PP (3.2% yr^{-1}) and chl a concentration (2.8% yr^{-1}) in the region over 1988–2013. The mean chl a value over the areas with MUPBs is also increasing, but the rate of increase is much smaller and statistically insignificant. The increase in phytoplankton growth and biomass is closely linked to an increase in light availability, as a result of decreasing sea ice (−1.9% yr^{-1}) and snow (−3.9% yr^{-1}) cover. The increase is also in response to an increase in nutrient availability in the upper 100 m, which is linked to enhanced air–sea exchange and strengthened upwelling and mixing in the water column in an ice-diminishing environment that facilitates an intensified Beaufort gyre (e.g., Proshutinsky et al., 2009; Yang, 2009; McLaughlin and Carmack, 2010; Zhang et al., 2010a; McPhee, 2013).

Model results further indicate the sporadic and patchy nature of MUPBs in the Chukchi Sea. The timing, location, and magnitude of MUPBs vary considerably in time and space, because of strong

spatiotemporal variations of light and nutrient availability. However, as observed during ICESCAPE, there is high probability of occurrence of MUPBs in the shelf break areas where enhanced nutrient concentration is simulated because of generally robust upwelling and other dynamic ocean processes in the shelf break areas such as mixing and horizontal advection (also see Pickart et al., 2013; Spall et al., 2014). This is particularly so in recent years with decreasing sea ice and snow cover such that enhanced light availability may reach the shelf break areas earlier to boost MUPBs there. Hence the simulated occurrence of MUPBs there is more frequent in the past decade than in the 1990s. The tendency to form MUPBs in the shelf break areas would only increase in the future if the sea ice and snow cover continues to decline and the Beaufort gyre continues to intensify, until at some point nutrient limitation starts to play a stronger role in the shelf break areas.

Acknowledgments

References

Andersen, O.G.N., 1989. Primary production, chlorophyll, light, and nutrients beneath the Arctic sea ice. In: Herman, Y. (Ed.), The Arctic Seas. Von Nostrand Reinhold, pp. 147–191.

Anderson, L.G., 1995. Chemical oceanography of the Arctic and its shelf seas. In: Smith Jr., W.O., Grebmeier, J.M. (Eds.), Arctic Oceanography: Marginal Ice Zones and Continental Shelves, Coastal Estuarine Studies, vol. 49. AGU, Washington, DC, pp. 183–202.

Arrigo, K.R., van Dijken, G., Pabi, S., 2008. Impact of a shrinking Arctic ice cover on marine primary production. Geophys. Res. Lett. 35, L19603. http://dx.doi.org/10.1029/2008GL035028.

Arrigo, K.R., et al., 2012. Massive phytoplankton blooms under Arctic sea ice. Science 336, 1408.

Arrigo, K.R., et al., 2014. Phytoplankton blooms beneath the sea ice in the Chukchi Sea. Deep-Sea Res. II.

Carmack, E., Wassmann, P., 2006. Food webs and physical–biological coupling on pan-Arctic shelves: unifying concepts and comprehensive perspectives. Prog. Oceanogr. 71, 446–477.

Carmack, E.C., Barber, D., Christensen, J., Macdonald, R., Rudel, B., Sakshaug, E., 2006. Climate variability and physical forcing of the food webs and the carbon budget on panarctic shelves. Prog. Oceanogr. 71 (2–4), 145–181.

Codispoti, L.A., Flagg, C., Kelly, V., Swift, J.H., 2005. Hydrographic conditions during the 2002 SBI process experiments. Deep-Sea Res. II 52, 3199–3226.

Codispoti, L.A., Kelly, V., Thessen, A., Matrai, P., Suttles, S., Hill, V.J., Steele, M., Light, B., 2013. Synthesis of primary production in the Arctic Ocean: III. Nitrate and phosphate based estimates of net community production. Prog. Oceanogr. 110, 126–150.

Comiso, J.C., 2012. Large decadal decline of the Arctic multilayer ice cover. J. Clim. 25, 1176–1193.

Fetterer, F., Untersteiner, N., 1998. Observations of melt ponds on Arctic sea ice. J. Geophys. Res. 103 (24), 821–24,835.

Frey, K.E., Perovich, D.K., Light, B., 2011. The spatial distribution of solar radiation under a melting Arctic sea ice cover. Geophys. Res. Lett. 38, L22501. http://dx.doi.org/10.1029/2011GL049241.

Garcia, H.E., Locarnini, R.A., Boyer, T.P., Antonov, J.I., 2006. World Ocean Atlas 2005, volume 4: nutrients (phosphate, nitrate, silicate). In: Levitus, S. (Ed.), NOAA Atlas NESDIS 64. U.S. Government Printing Office, Washington, DC, p. 396.

Gill, A., 1982. Atmosphere-Ocean Dynamics. International Geophysics Series, vol. 30. Academic Press Inc..

Gosselin, M., Levasseur, M., Wheeler, P.E., Horner, R.A., Booth, B.C., 1997. New measurements of phytoplankton and ice algal production in the Arctic Ocean. Deep-Sea Res. II 44, 1623–1644.

Grebmeier, J.M., Harvey, H.R., 2005. The Western Arctic Shelf–Basin Interactions (SBI) project: an overview. Deep-Sea Res. II 52, 3109–3115.

Grenfell, T.C., Maykut, G.A., 1977. The optical properties of ice and snow in the Arctic. Basin. J. Glaciol. 18, 445–463.

Haas, C., Lobach, J., Hendricks, S., Rabenstein, L., Pfaffling, A., 2009. Helicopter-borne measurements of sea ice thickness, using a small and lightweight, digital EM system. J. Appl. Geophys. 67 (3), 234–241.

Hibler III, W.D., 1980. Modeling a variable thickness sea ice cover. Mon. Weather Rev. 108, 1943–1973.

Hill, V., Cota, G., 2005. Spatial patterns of primary production on the shelf, slope and basin of the Western Arctic in 2002. Deep-Sea Res. II 52, 3344–3354.

Holland, D.M., 2000. Merged IBCAO/ETOPO5 global topographic data product. National Geophysical Data Center (NGDC), Boulder CO. ⟨http://www.ngdc.noaa.gov/mgg/bathymetry/arctic/ibcaorelatedsites.html⟩.

Kalnay, E., et al., 1996. The NCEP/NCAR 40-year reanalysis project. Bull. Am. Meteorol. Soc. 77, 437–471.

Kay, J.E., L'Ecuyer, T., Gettelman, A., Stephens, G., O'Dell, C., 2008. The contribution of cloud and radiation anomalies to the 2007 Arctic sea ice extent minimum. Geophys. Res. Lett. 35, L08503. http://dx.doi.org/10.29/2008GL033451.

Kishi, M.J., Kashiwai, M., Ware, D.M., Megrey, B.A., Eslinger, D.L., Werner, F.E., Noguchi-Aita, M., Azumaya, T., Fujii, M., Hashimoto, S.i., Huang, D., Iizumi, H., Ishida, Y., Kang, S.g., Kantakov, G.A., Kim, H.-C., Komatsu, K., Navrotsky, V.V., Smith, S.L., Tadokoro, K., Tsuda, A., Yamamura, O., Yamanaka, Y., Yokouchi, K., Yoshie, N., Zhang, J., Yury, I.Z., Zvalinsky, V.I., 2007. NEMURO – a lower trophic level model for the North Pacific marine ecosystem. Ecol. Model. 202, 12–25.

Krishfield, R.A., Proshutinsky, A., Tateyama, K., Williams, W.J., Carmack, E.C., McLaughlin, F.A., Timmermans, M.-L., 2014. Deterioration of perennial sea ice in the Beaufort Gyre from 2003 to 2012 and its impact on the oceanic freshwater cycle. J. Geophys. Res. Ocean. 119, 1271–1305. http://dx.doi.org/10.1002/2013JC008999.

Kurtz, N.T., Farrell, S.L., Studinger, M., Galin, N., Harbeck, J.P., Lindsay, R., Onana, V.D., Panzer, B., Sonntag, J.G., 2013. Sea ice thickness, freeboard, and snow depth products from Operation IceBridge airborne data. Cryosphere 7, 1035–1056. http://dx.doi.org/10.5194/tc-7-1035-2013.

Kwok, R., 2007. Near zero replenishment of the Arctic multiyear sea ice cover at the end of 2005 summer. Geophys. Res. Lett. 34, L05501. http://dx.doi.org/10.1029/2006GL028737.

Lavoie, D., Macdonald, R.W., Denman, K.L., 2009. Primary productivity and export fluxes on the Canadian shelf of the Beaufort Sea: a modeling study. J. Mar. Syst. 75, 17–32.

Lee, S.H., Whitledge, T.E., 2005. Primary and new production in the deep Canada Basin during summer 2002. Polar Biol. 28, 190–197.

Light, B., Grenfell, T.C., Perovich, D.K., 2008. Transmission and absorption of solar radiation by Arctic sea ice during the melt season. J. Geophys. Res. 113, CO3023. http://dx.doi.org/10.1029/2006JC003977.

Lindsay, R.W., Zhang, J., 2006. Assimilation of ice concentration in an ice-ocean model. J. Atmos. Ocean. Tech. 23, 742–749.

Lindsay, R.W., 2010. Unified Sea Ice Thickness Climate Data Record, Polar Science Center, Applied Physics Laboratory, University of Washington. http://psc.apl.washington.edu/sea_ice_cdr/, digital media.

Lindsay, R., 2013. Unified Sea Ice Thickness Climate Data Record Collection Spanning 1947–2012. National Snow and Ice Data Center, Boulder, Colorado USA. 10.7265/N5D50JXV.

Lowry, K., van Dijken, G.L., Arrigo, K.R., 2014. Evidence of under-ice phytoplankton blooms in the Chukchi Sea from 1998 to 2012. Deep-Sea Res. II.

Manda, A., Hirose, N., Yanagi, T., 2005. Feasible method for the assimilation of satellite-derived SST with an ocean circulation model. J. Atmos. Ocean. Technol. 22 (6), 746–756. http://dx.doi.org/10.1175/JTECH1744.1.

Marchuk, G.I., Kagan, B.A., 1989. Dynamics of Ocean Tides. Kluwer Academic Publishers p. 327.

Maslanik, J.A., Fowler, C., Stroeve, J., Drobot, S., Zwally, J., Yi, D., Emery, W., 2007. A younger, thinner Arctic ice cover: increased potential for rapid, extensive sea-ice loss. Geophys. Res. Lett. 34, L24501. http://dx.doi.org/10.29/2007GL032043.

Maslanik, J., Stroeve, J., Fowler, C., Emery, W., 2011. Distribution and trends in Arctic sea ice age through spring 2011. Geophys. Res. Lett. 34, L13502. http://dx.doi.org/10.29/2007GL032043.

Maykut, G.A., Untersteiner, N., 1971. Some results from a time-dependent thermo-dynamic model of sea ice. J. Geophys. Res. 76, 1550–1575.

Melling, H., Riedel, D.A., 2008. Ice Draft and Ice Velocity Data in the Beaufort Sea, 1990–2003. National Snow and Ice Data Center, Boulder, Colorado USA.

McLaughlin, F.A., Carmack, E.C., 2010. Deepening of the nutricline and chlorophyll maximum in the Canada Basin interior, 2003–2009. Geophys. Res. Lett. 37, L24602. http://dx.doi.org/10.1029/2010GL045459.

McPhee, M.G., 2013. Intensification of geostrophic currents in the Canada Basin, Arctic Ocean. J. Clim. 26, 3130–3138. http://dx.doi.org/10.1175/JCLI-D-12-00289.1.

Mundy, C.J., Gosselin, J., Ehn, J., Gratton, Y., Rossnagel, A., Barber, D.G., Martin, J., Tremblay, J.É., Plamer, M., Arrigo, K.R., Darnis, G., Fortier, L., Else, B., Papkyriakou, T., 2009. Contribution of under-ice primary production ot an ice-edge upwelling phytoplankton bloom in the Canaidan Beaufort Sea. Geophys. Res. Lett. 36, L17601. http://dx.doi.org/10.29/2009GL038837.

Nicolaus, M., Katlein, C., Maslanik, J., Hendricks, S., 2012. Changes in Arctic sea ice result in increasing light transmittance and absorption. Geophys. Res. Lett. 39, L24501. http://dx.doi.org/10.1029/2012GL053738.

Overland, J.E., Francis, J.A., Hanna, E., Wang, M., 2012. The recent shift in early summer Arctic atmospheric circulation. Geophys. Res. Lett. 39, L19804. http://dx.doi.org/10.29/2011GL047735.

Parkinson, C.L., Washington, W.M., 1979. A large-scale numerical model of sea ice. J. Geophys. Res. 84, 311–337.

Palmer, M.A., Saenz, B.T., Arrigo, K.R., 2014. Impacts of sea ice retreat, thinning, and melt-pond proliferation on the summer phytoplankton bloom in the Chukchi Sea, Arctic Ocean. Deep-Sea Res. II.

Parkinson, C.L., Comiso, J.C., 2013. On the 2012 record low Arctic sea ice cover: combined impact of preconditioning and August storm. Geophys. Res. Lett. 40, 1356–1361. http://dx.doi.org/10.1002/grl.50349.

Perovich, D.K., Richter-Menge, J.A., Jones, K.F., Light, B., 2008. Sunlight, water, and ice: extreme Arctic sea ice melt during the summer of 2007. Geophys. Res. Lett. 35, L11501. http://dx.doi.org/10.1029/2008GL034007.

Pickart, R.S., Moore, G.W.K., Torres, D.J., Fratantoni, P.S., Goldsmith, R.A., Yang, J., 2009. Upwelling on the continental slope of the Alaskan Beaufort Sea: storms, ice, and oceanographic response. J. Geophys. Res. 114, C00A13. http://dx.doi.org/10.1029/2208JC005.

Pickart, R.S., Spall, M.A., Moore, G.W.K., Weingartner, T.J., Woodgate, R.A., Aagaard, K., Shimada, K., 2011. Upwelling in the Alaskan Beaufort Sea: atmospheric forcing and local versus non-local response. Prog. Oceanogr. 88, 78–100.

Pickart, R.S., Schulze, L.M., Moore, G.W.K., Charette, M.A., Arrigo, K.R., van Dijken, G., Danielson, S.L., 2013. Long-term trends of upwelling and impacts on primary productivity in the Alaskan Beaufort Sea. Deep-Sea Res. I 79, 106–121.

Pinker, R.T., Laszlo, I., 1992. Global distribution of photosynthetically active radiation as observed from satellites. J. Clim. 5, 56–65.

Proshutinsky, A., Krishfield, R., Timmermans, M.-L., Toole, J., Carmack, E., McLaughlin, F., Williams, W.J., Zimmermann, S., Itoh, M., Shimada, K., 2009. Beaufort Gyre freshwater reservoir: state and variability from observations. J. Geophys. Res. 114, C00A10. http://dx.doi.org/10.1029/2008JC005104.

Redfield, A.C., Ketchum, B.H., Richards, F.A., 1963. The influence of organisms on the composition of sea-water. In: Hill, M.N. (Ed.), The Sea. Wiley-Interscience, New York, pp. 26–77.

Rothrock, D.A., Percival, D.B., Wensnahan, M., 2008. The decline in arctic sea-ice thickness: separating the spatial, annual, and interannual variability in a quarter century of submarine data. J. Geophys. Res. 113 (C5), C05003.

Schweiger, A., Lindsay, R.W., Zhang, J., Steele, M., Stern, H., Kwok, R., 2011. Uncertainty in modeled Arctic sea ice volume. J. Geophys. Res. 116, C00D06. http://dx.doi.org/10.1029/2011JC007084.

Serreze, M.C., Holland, M.,M., Stroeve, J., 2007. Perspectives on the Arctic's shrinking sea-ice cover. Science 315, 1533–1536.

Smith, R.D., Dukowicz, J.K., Malone, R.C., 1992. Parallel ocean general circulation modeling. Physica D 60, 38–61.

Smith, W.O., Sakshaug, E., 1990. Polar phytoplankton. In: Smith, W.O. (Ed.), Polar Oceanography, Part B. Academic, San Diego, pp. 475–525.

Spall, M.A., Pickart, R.S., Brugler, E.T., Moore, G.W.K., Thomas, L., Arrigo, K.R., 2014. Role of shelfbreak upwelling in the formation of a massive under-ice bloom in the Chukchi Sea. Deep-Sea Res. II.

Steele, M., Zhang, J., Ermold, W., 2010. Mechanisms of summertime upper Arctic Ocean warming and the effect on sea ice melt. J. Geophys. Res. 115, http://dx.doi.org/10.1029/2009JC005849C11004 , http://dx.doi.org/10.1029/2009JC005849.

Stroeve, J.C., Serreze, M.C., Holland, M.M., Kay, J.E., Maslanik, J., Barrett, A.P., 2012. The Arctic's rapidly shrinking ice cover: a research synthesis. Clim. Change 110 (3), 1005–1027.

Weingartner, T., Aagaard, K., Woodgate, R., Danielson, S., Sasaki, Y., Cavalieri, D., 2005. Circulation on the north central Chukchi Sea shelf. Deep-Sea Res. II 52, 3150–3174.

Witte, H., Fahrbach, E., 2005. AWI Moored ULS Data, Greenland Sea and Fram Strait, 1991–2002. National Snow and Ice Data Center.

Woodgate, R.A., Aagaard, K., Swift, J.H., Falkner, K.K., Smethie, W.M., 2005. Pacific Ventilation of the Arctic Ocean's lower halocline by upwelling and diapycnal mixing over the continental margin. Geophys. Res. Lett. 32, L18609. http://dx.doi.org/10.1029/2005GL023999.

Yang, J., 2009. Seasonal and interannual variability of downwelling in the Beaufort Sea. J. Geophys. Res. 114, C00A14. http://dx.doi.org/10.1029/2008JC005084.

Zhang, J., Rothrock, D.A., 2003. Modeling global sea ice with a thickness and enthalpy distribution model in generalized curvilinear coordinates. Mon. Weather Rev. 131 (5), 681–697.

Zhang, J., 2005. Warming of the arctic ice-ocean system is faster than the global average since the 1960s. Geophys. Res. Lett. 32, L19602. http://dx.doi.org/10.1029/2005GL024216.

Zhang, J., Steele, M., 2007. The effect of vertical mixing on the Atlantic water layer circulation in the Arctic Ocean. J. Geophys. Res. 112, C04S04. http://dx.doi.org/10.1029/2006JC003732.

Zhang, J., Lindsay, R.W., Steele, M., Schweiger, A., 2008. What drove the dramatic retreat of Arctic sea ice during summer 2007? Geophys. Res. Lett. 35, L11505. http://dx.doi.org/10.1029/2008GL034005.

Zhang, J., Spitz, Y.H., Steele, M., Ashjian, C., Campbell, R., Berline, L., Matrai, P., 2010a. Modeling the impact of declining sea ice on the Arctic marine planktonic ecosystem. J. Geophys. Res. 115, C10015. http://dx.doi.org/10.1029/2009JC005387.

Zhang, J., Woodgate, R., Moritz, R., 2010b. Sea ice response to atmospheric and oceanic forcing in the Bering Sea. J. Phys. Oceanogr. 40, 1729–1747. http://dx.doi.org/10.1175/2010JPO4323.1.

Zhang, J., Lindsay, R., Schweiger, A., Steele, M., 2013. The impact of an intense summer cyclone on 2012 Arctic sea ice retreat. Geophys. Res. Lett. 40, 1–7. http://dx.doi.org/10.1002/grl.50190.

Zhang, J., Ashjian, C., Campbell, R., Hill, V., Spitz, Y.H., Steele, M., 2014. The great 2012 Arctic Ocean summer cyclone enhanced biological productivity on the shelves. J. Geophys. Res. 119, 1–16. http://dx.doi.org/10.1002/2013JC009301.